Synthetic Aperture Sequential Beamforming

Kortbek, Jacob; Jensen, Jørgen Arendt; Gammelmark, Kim Løkke

Published in:
2008 IEEE International Ultrasonics Symposium

Link to article, DOI:
10.1109/ULTSYM.2008.0233

Publication date:
2008

Digital Object Identifier: 10.1109/ULTSYM.2008.0233

Synthetic Aperture Sequential Beamforming

Jacob Kortbek*, Jørgen Arendt Jensen†, Kim Løkke Gammelmark*
*BK Medical, Mileparken 34, 2730 Herlev, Denmark, Email: jbk@bkmed.dk
†Technical University of Denmark, Center for Fast Ultrasound Imaging, 2800, Kgs. Lyngby, Denmark

***Abstract*—A synthetic aperture focusing (SAF) technique denoted Synthetic Aperture Sequential Beamforming (SASB) suitable for 2D and 3D imaging is presented. The technique differ from prior art of SAF in the sense that SAF is performed on pre-beamformed data contrary to channel data. The objective is to improve and obtain a more range independent lateral resolution compared to conventional dynamic receive focusing (DRF) without compromising frame rate. SASB is a two-stage procedure using two separate beamformers. First a set of B-mode image lines using a single focal point in both transmit and receive is stored. The second stage applies the focused image lines from the first stage as input data. The SASB method has been investigated using simulations in Field II and by off-line processing of data acquired with a commercial scanner. The performance of SASB with a static image object is compared with DRF. For the lateral resolution the improvement in FWHM equals a factor of 2 and the improvement at -40 dB equals a factor of 3. With SASB the resolution is almost constant throughout the range. The resolution in the near field is slightly better for DRF. A decrease in performance at the transducer edges occur for both DRF and SASB, but is more profound for SASB.**

I. Introduction

In synthetic transmit aperture (STA) imaging a single element is used to transmit a spherical wave, and RF-samples from a multi-element receive aperture are stored. Delay-and-sum (DAS) beamforming can be applied to these data to construct a low-resolution image (LRI). Several emissions from single elements across the aperture will synthesize a larger aperture and the LRI's from these emissions can be added into a single high-resolution image (HRI). The HRI is dynamically focused in both transmit and receive yielding an improvement in resolution [1]. This imaging technique sets high demands on processing capabilities, data transport, and storage and makes implementation of a full SA system very challenging and costly.

Mono-static synthetic aperture focusing (SAF) can be applied to imaging with a mechanically focused concave element [2]. This technique combined with the concept of using a focal point as a virtual source (VS) [3]–[7] is the foundation for the technique presented in this paper.

In this paper a SAF technique denoted Synthetic Aperture Sequential Beamforming (SASB) is presented. The technique differ from prior art of SAF in the sense that SAF is performed on pre-beamformed data contrary to channel data, and eliminates the need for storing LRI's. This is an important issue in terms of implementation complexity. Especially in applications such as 2D-array imaging, and 3D imaging in general, where the demand for data transport and beamforming is massive. The technique consists of two sequential beamforming stages and a memory for storage of intermediate image lines from the first stage beamformer (BF1). BF1 is of low complexity, since it only requires the calculation of a single delay-profile. The second stage beamformer (BF2) apply the output lines from BF1 as input data, and has the complexity of a general dynamic receive focusing beamformer. The objective is to improve and obtain a more range independent resolution compared to conventional ultrasound imaging, with a downscaled system complexity compared to STA, and without compromising frame rate. The method is investigated using a linear array, and a static image object.

A. Method

SASB is a two-stage delay-and-sum beamforming procedure, which can be applied to B-mode imaging with any array transducer. The initial step is to construct and store a set of B-mode image lines using a conventional sliding sub-aperture. These 1st stage lines are obtained with a single focal point in both transmit and receive. These focal points are preferably coincident. The second stage consist of an additional beamformer using the focused RF-data from the output of BF1 as input data. For each new emission a new BF1 line is created and stored in a first-in-first-out (FIFO) buffer, and a new BF2 line is created based on the content of the FIFO. This yields a frame rate which is at least equal to DRF. The number of channels in BF2 also determines the required size of the FIFO and has a direct influence on the performance.

The transmit focal point is considered as a virtual source (VS) emitting a spherical wave front spatially confined by the opening angle. BF1 has a fixed receive focus and this focal point is considered as a virtual receiver (VR). When the VS and the VR coincide the focal point can be considered as a virtual transducer element (VE). The focusing delays for BF1 are found from the round trip time-of-flight (TOF), which is the propagation time of the emitted wave in its path from the transmit origin, to the image point (IP), $\vec{r}_{ip}$ and return to the receiver. When the VS and the VR coincide at the position $\vec{r}_{ve}$ the TOF is calculated in accordance with Fig. 1, where the VE is included in the TOF path. Assuming the speed of sound c is known, the delay value, t_d is calculated as $t_d = d_{tof}/c$, where d_{tof} is the length of the TOF path. With the receiving element at position $\vec{r}_r$ the path length is

$$\begin{aligned} d_{tof} &= |\vec{r}_{ve} - \vec{r}_e| \pm |\vec{r}_{ip} - \vec{r}_{ve}| \pm |\vec{r}_{ve} - \vec{r}_{ip}| + |\vec{r}_r - \vec{r}_{ve}| \\ &= z_v \pm 2z_{vf} + |\vec{r}_r - \vec{r}_{ve}| \end{aligned} \quad (1)$$

z_v is the distance from the aperture to the VE, and z_{vf} is the distance from the VE to the IP. The $\pm$ in (1) refer to whether the IP is above or below the VE. Notice that the differences between the individual channel delays does not change with the position of IP as in DRF since the term involving the receive elements, $|\vec{r}_r - \vec{r}_{ve}|$ does not dependent on $\vec{r}_{ip}$. BF1 is of low complexity since only a single set of delay values must be calculated.

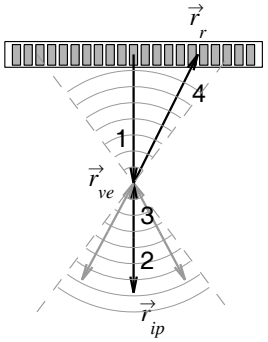

Fig. 1. The time-of-flight path for calculating the BF1 receive delay for the element at $\vec{r}_r$ and for the image point $\vec{r}_{ip}$ when fixed receive focusing is applied. The transmit focal point and the fixed receive focal point coincide and form a virtual transducer element (VE) at $\vec{r}_{ve}$. The total length of the time-of-flight path is the sum of the length of the four arrows.

With fixed receive focusing each point in the focused image line from BF1 contains information from a set of spatial positions. These are defined by the arc of a circle limited by the opening angle that crosses the image point and has a center in the focal point as illustrated in Fig. 2. In this figure a single sample on each line from BF1 is indicated with a dot. Each sample contains information from many image points indicated by bold arcs, but only from one common image point. This is where the arcs intersect, and these samples can be summed coherently. In general a single image point is therefore represented in multiple BF1 image lines obtained from multiple emissions. This is exploited in BF2, where each output sample is constructed by selecting a sample from each of those output lines from BF1, which contain information from the spatial position of the image point and summing a weighted set of these samples. The construction of a high resolution image point at $\vec{r}_{ip} = (x,z)$ can be formulated as a sum over samples from the $K(z)$ contributing emissions

$$h(\vec{r}_{ip}) = \sum_{k=1}^{K(z)} \mathcal{W}(x_k,z)s_k(z_k)\,. \tag{2}$$

The spatial RF-signal from the output of BF1 for emission k is denoted s_k, and z_k is the depth of the contributing sample. This index is calculated as a direct consequence of the focusing in BF1 formulated in (1), and illustrated in Fig. 1 and Fig. 2.

$$\begin{aligned} z_k =& |\vec{r}_{ve_k} - \vec{r}_{e_k}| \pm |\vec{r}_{ip} - \vec{r}_{ve_k}| \pm |\vec{r}_{ve_k} - \vec{r}_{ip}| + |\vec{r}_{e_k} - \vec{r}_{ve_k}| \\ =& 2z_v \pm 2z_{vf_k} \end{aligned} \tag{3}$$

The sub-index k indicate affiliation to emission number k. The variable $\mathcal{W}$ in (2) is a dynamic apodization function. It controls the weighting of the contribution from each emission. It is a function of the axial position of the image point, z since the number of contributing emissions, $K(z)$ increases with range. The VE's of the contributing emissions form a synthetic aperture. $K(z)$ is a measure of the size of the synthesized aperture, and since K increases linearly with range within the boundary of the physical transducer it facilitates a range independent lateral resolution. $K(z)$ can be calculated directly from the geometry shown in Fig. 3 as

$$K(z) = \frac{L(z)}{\Delta} = \frac{2(z-z_v)\tan(\alpha/2)}{\Delta}\,. \tag{4}$$

The variable $L(z)$ is the lateral width of the wave field at depth, z, and Δ is the distance between the VE's of two consecutive emissions. $\alpha = 2\arctan\frac{1}{2F\#}$ is the opening angle of the VE. The F-number is $F\# = z_v/L_A$, where L_A is the size of the sub-aperture. The opening angle is the angular span for which the phase of the wave field can be considered constant [8].

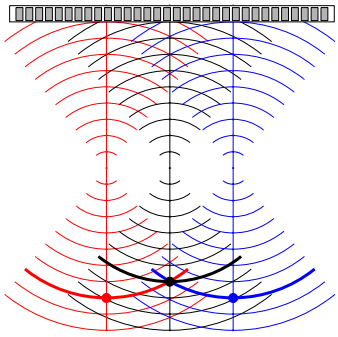

Fig. 2. Example of wave propagation and BF1 image lines from 3 different emissions. Each point on the image lines contains information from the spatial positions indicated by the bold arcs. A single high resolution image point is obtained by extracting information from all of those BF1 image lines which contain information from that image point.

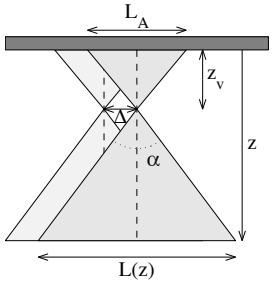

Fig. 3. Geometry model of the emitted wave fields from two consecutive emissions. The lateral width, $L(z)$ of the wave field at a depth, z determines the number of LRL's which can be added in the 2nd stage beamformer for an image point at depth, z.

The formulation of the method in this section assumes an aperture with an infinite number of elements. This becomes apparent when observing (4). At greater depth $K(z)$ will exceed the number of available BF1 lines. At depths beyond this point

the synthesized aperture will no longer increase with depth and the lateral resolution will no longer be range independent. Another consequence of a limited element count is that the number of emissions that can be applied in the sum in (2) decreases as the lateral position of the image point moves away from the center. The synthesized aperture decreases for image lines near the edges, and the lateral resolution is, thus, laterally dependent. The formulation also assumes that the image object is stationary during all transmission, which is not the case in-vivo. Tissue motion and motion artifacts are nevertheless not completely destructive to SA imaging. Motion estimation and the susceptibility to motion of SA imaging has been investigated by several authors [9]–[14], and techniques to address the problems with tissue motion have been demonstrated.

Grating lobes arise at a combination of a sparse spatial sampling and wave fields with large incident angles. The input data for the SAF in BF2 are the image lines from BF1, and the construction of these lines is deciding for the presence of grating lobes. The VE's form a virtual array and the distance between the VE's, Δ determines the lateral spatial sampling. The range of incident angles to the virtual array can be determined by the opening angle, α of the VE. By restricting α a sample of a BF1 line only contains information from wave fields with incident angles within α. The grating lobes can be avoided by adjusting either of both of these parameters. If $\lambda = c/f_0$, where f_0 is the center frequency, the narrow band condition for avoiding grating lobes can formulated as

$$F\# \geq \frac{\Delta}{\lambda/2}. \tag{5}$$

II. Results

The performance of SASB is primarily dependent on the VE position and $F\#$. These parameters also determine the number of elements used during transmission, and has an influences on the emitted energy and the signal to noise ratio. For a comparison with conventional DRF, a VE at 20 mm and $F\# = 1.5$ has been chosen. Various applied parameters are listed in Table I.

Parameter	Value
Sampling frequency	120 MHz
Pitch	0.21 mm
Center frequency	7 MHz
Number of elements	191
BF1, Number of channels, tx/rx	63
BF1, Apodization, tx/rx	Hamming
BF1, Focal depth (virtual element)	20 mm
BF1, Number of lines/VE	191
BF2, Number of channels	$N_{ch} \leq 191$
BF2, Apodization	Hamming
BF2, Number of lines	191

TABLE I
APPLIED VALUES FOR THE SIMULATIONS IN FIELD II AND SASB PROCESSING.

Fig. 4 shows images with DRF and SASB side by side, and Fig. 5 shows the quantified lateral resolution for different configurations. The quantified axial resolution does not differ between the different configurations and is not shown. Different positions of the transmit focal point in DRF has been applied for a fair comparison. In Fig. 4 the number of channels in the 2nd stage beamformer is $N_{ch} = 191$. In Fig. 5 SASB results are presented where the number of channels has been limited to $N_{ch} = 127$, and $N_{ch} = 63$.

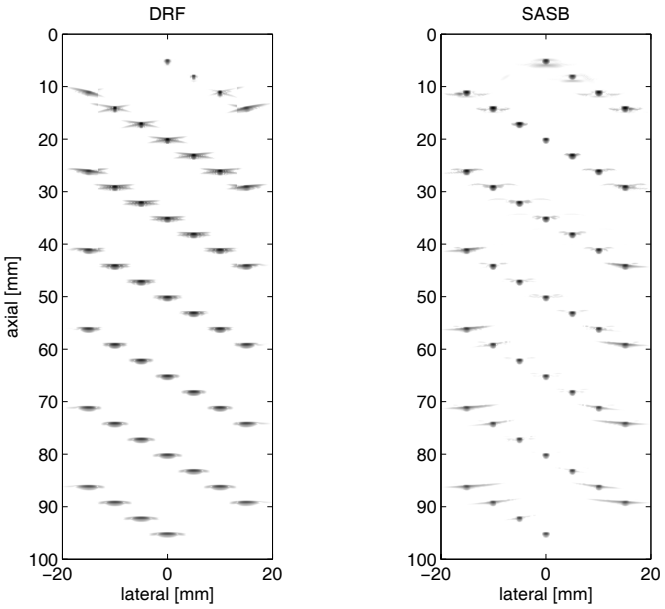

Fig. 4. Simulated image of point targets. DRF with transmit focus at 70 mm (left), and SASB (Right). Dynamic Range is 60 dB

There is an substantial improvement in resolution using SASB compared to DRF. The improvement in FWHM equals a factor of 2 and the improvement at -40 dB equals a factor of 3. The improvement of SASB over DRF is a reality except for a few exceptions in the given example. At depths until 20 mm the FWHM is superior with DRF. With SASB the resolution is almost constant throughout the range. For DRF the FWHM increases almost linearly with range and the resolution at -40 dB is fluctuating with range.

By putting restrictions on the number of 2nd stage beamformer channels the system complexity is reduced. It will have a negative consequence on resolution, since the synthesized aperture decreases. Both the FWHM and the resolution at -40 dB cease to be constant at the depth at which synthetic aperture ceases to expand. When the number of channels is restricted to $N_{2nd} = 63$ the performance of SASB is still superior to DRF.

A commercial scanner and a linear array transducer with parameters similar to the ones in Table I have been used to acquire data. A tissue phantom with wire targets and 0.5 dB/MHz/cm attenuation is used as imaging object. 2nd stage SASB processing, envelope detection, and logarithmic compression is done off-line for both DRF and SASB. A side by side comparison between the DRF image and the SASB image is shown in Fig. 6.

At the center of the image the resolution of SASB is superior

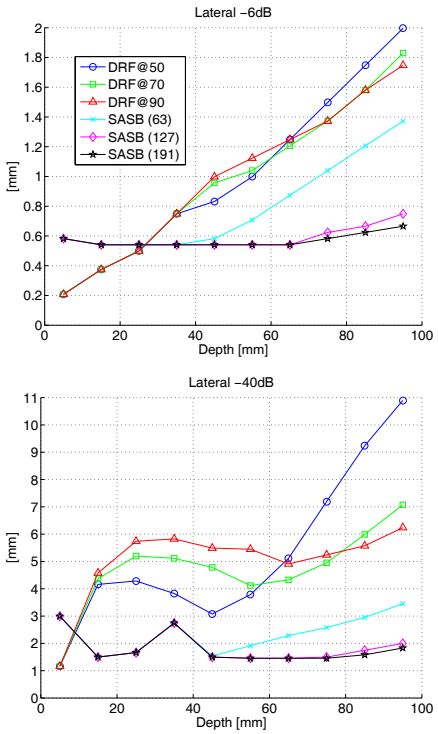

Fig. 5. Lateral resolution of DRF and SASB as function of depth at -6 dB (top) and -40 dB (bottom). For DRF the transmit focal point is at 50 mm, 70 mm, and 90 mm. SASB results are presented using different number of BF2 channels. $N_{ch} = 63$, $N_{ch} = 127$, and $N_{ch} = 191$.

to DRF and is practically range independent. The resolution in the near field is slightly better for DRF.

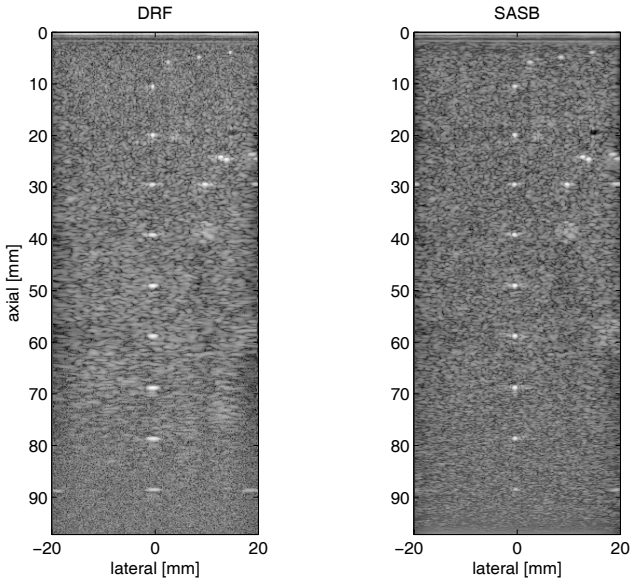

Fig. 6. Measured data. DRF with transmit focus at 65 mm (left), and SASB (Right). Dynamic Range is 60 dB

III. Conclusion

The SASB method has been investigated using simulations in Field II and by off-line processing of data acquired with a commercial scanner, and lateral resolution is compared with DRF. At the image center the improvement in FWHM equals a factor of 2 and the improvement at -40 dB equals a factor of 3. The resolution decreases at the image edges. Contrary to DRF, the resolution is almost constant throughout the range with SASB. The resolution in the near field is slightly better for DRF. A decrease in performance at the transducer edges occur for both DRF and SASB, but is more profound for SASB. SASB is a promising SA technique with an implementation of low complexity. The technique offers great flexibility in the compromise between implementation complexity, resolution and frame rate. The susceptibility to motion is a topic of future investigation.

References

[1] J. T. Ylitalo and H. Ermert. Ultrasound synthetic aperture imaging: monostatic approach. *IEEE Trans. Ultrason., Ferroelec., Freq. Contr.*, 41:333–339, 1994.

[2] J. Kortbek, J. A. Jensen, and K. L. Gammelmark. Synthetic Aperture Focusing Applied to Imaging Using a Rotating Single Element Transducer. In *Proc. IEEE Ultrason. Symp.*, Oct. 2007 (Accepted).

[3] C. Passmann and H. Ermert. A 100-MHz ultrasound imaging system for dermatologic and ophthalmologic diagnostics. *IEEE Trans. Ultrason., Ferroelec., Freq. Contr.*, 43:545–552, 1996.

[4] C. H. Frazier and W. D. O'Brien. Synthetic aperture techniques with a virtual source element. *IEEE Trans. Ultrason., Ferroelec., Freq. Contr.*, 45:196–207, 1998.

[5] S. I. Nikolov and J. A. Jensen. Virtual ultrasound sources in high-resolution ultrasound imaging. In *Proc. SPIE - Progress in biomedical optics and imaging*, volume 3, pages 395–405, 2002.

[6] S. I. Nikolov and J. A. Jensen. 3D synthetic aperture imaging using a virtual source element in the elevation plane. In *Proc. IEEE Ultrason. Symp.*, volume 2, pages 1743–1747, 2000.

[7] M. H. Bae and M. K. Jeong. A study of synthetic-aperture imaging with virtual source elements in B-mode ultrasound imaging systems. In *IEEE Trans. Ultrason., Ferroelec., Freq. Contr.*, volume 47, pages 1510–1519, 2000.

[8] N. Oddershede and J. A. Jensen. Effects influencing focusing in synthetic aperture vector flow imaging. *IEEE Trans. Ultrason., Ferroelec., Freq. Contr.*, 54(9):1811–1825, September 2007.

[9] G. E. Trahey and L. F. Nock. Synthetic receive aperture imaging with phase correction for motion and for tissue inhomogenities - part II: effects of and correction for motion. *IEEE Trans. Ultrason., Ferroelec., Freq. Contr.*, 39:496–501, 1992.

[10] M. Karaman, H. Ş. Bilge, and M. O'Donnell. Adaptive multi-element synthetic aperture imaging with motion and phase aberation correction. *IEEE Trans. Ultrason., Ferroelec., Freq. Contr.*, 42:1077–1087, 1998.

[11] C. R. Hazard and G. R. Lockwood. Effects of motion artifacts on a synthetic aperture beamformer for real-time 3D ultrasound. In *Proc. IEEE Ultrason. Symp.*, pages 1221–1224, 1999.

[12] J. S. Jeong, J. S. Hwang, M. H. Bae, and T. K. Song. Effects and limitations of motion compensation in synthetic aperture techniques. In *Proc. IEEE Ultrason. Symp.*, pages 1759 –1762, 2000.

[13] S. I. Nikolov and J. A. Jensen. K-space model of motion artifacts in synthetic transmit aperture ultrasound imaging. In *Proc. IEEE Ultrason. Symp.*, pages 1824–1828, 2003.

[14] K. L. Gammelmark and J. A. Jensen. Duplex synthetic aperture imaging with tissue motion compensation. In *Proc. IEEE Ultrason. Symp.*, pages 1569–1573, 2003.